

# Mechanical Properties and Stacking Fault Energies of NiFeCrCoMn High-Entropy Alloy

A.J. ZADDACH,<sup>1</sup> C. NIU,<sup>1</sup> C.C. KOCH,<sup>1</sup> and D.L. IRVING<sup>1,2</sup>

1.—Department of Materials Science and Engineering, North Carolina State University, Raleigh, NC 27695-7907, USA. 2.—e-mail: ddirving@ncsu.edu

Materials with low stacking fault energies have been long sought for their many desirable mechanical attributes. Although there have been many successful reports of low stacking fault alloys (for example Cu-based and Mg-based), many have lacked sufficient strength to be relevant for structural applications. The recent discovery and development of multicomponent equiatomic alloys (or high-entropy alloys) that form as simple solid solutions on ideal lattices has opened the door to investigate changes in stacking fault energy in materials that naturally exhibit high mechanical strength. We report in this article our efforts to determine the stacking fault energies of two- to five-component alloys. A range of methods that include ball milling, arc melting, and casting, is used to synthesize the alloys. The resulting structure of the alloys is determined from x-ray diffraction measurements. First-principles electronic structure calculations are employed to determine elastic constants, lattice parameters, and Poisson's ratios for the same alloys. These values are then used in conjunction with x-ray diffraction measurements to quantify stacking fault energies as a function of the number of components in the equiatomic alloys. We show that the stacking fault energies decrease with the number of components. Nonequiatomically alloys are also explored as a means to further reduce stacking fault energy. We show that this strategy leads to a means to further reduce the stacking fault energy in this class of alloys.

## INTRODUCTION

In many conventional structural materials, strength and ductility are mutually exclusive. When the strength is increased, such as by refining the grain size, there often is a corresponding decrease in ductility, which limits the use of the strengthened material for structural applications.<sup>1</sup> In ultrafine grain (UFG) and nanocrystalline (NC) materials, this is attributed to their poor capacity for accumulating dislocations in the small grains, resulting in a lack of work hardening.<sup>1,2</sup> Recently, significant advances have been made in developing UFG/NC materials with improved ductility by selecting alloys with low stacking fault energy (SFE).<sup>1-7</sup> High SFE materials deform by dislocation glide and dissociation into partial dislocations is difficult. In low SFE materials, dissociation into partial dislocations is more energetically favorable and the spacing between the partial dislocations (the width of the stacking fault) is larger. As the spacing increases,

cross-slip and climb becomes more difficult, increasing strength. Low SFE materials are also more likely to deform by twinning, increasing dislocation storage capacity, strain hardening rate, and ductility.<sup>2-5,8</sup> High-density "bundles" of nanoscale twins have been observed after deformation in low SFE copper alloys.<sup>9</sup> Regions containing high densities of nanoscale-spaced stacking faults that provide a similar strengthening effect have been observed in low SFE magnesium alloys.<sup>10</sup>

To date, much of the research on improving strength and ductility by reducing SFE has focused on binary and ternary Cu-based alloys and multicomponent Mg-based alloys. The main reason for this attention is the well-established ability of some alloying elements to form solid solutions in Cu and Mg and to significantly lower the SFE. While some impressive results have been obtained, the strength of most of the alloys is still relatively low. Cu-10 wt.% Zn with a grain size of 110 nm retains elongation to failure of greater than 6%, but the yield strength is

improved to only  $\sim 600$  MPa.<sup>1</sup> An alternative, and a possibly more desirable system, would be one that, like the Cu-based alloys, can form a face-centered cubic (fcc) solid solution over a wide range of compositions and has low SFE but also retains high intrinsic strength.

Recently, a new class of multicomponent alloy systems has been developed in which the design is based not on adding solutes to a single “base” element but rather on choosing elements that will form solid solutions when mixed at near-equiatomic concentrations. These high-entropy alloys (HEAs) meet these criteria and are found to form solid solutions. This behavior has been attributed to the large configurational entropy when five or more elements at near-equiatomic ratios are mixed together.<sup>11</sup> The elements likely to form as an HEA solid solution and which lattice is likely to form will now be briefly reviewed.

A fundamental understanding of the mechanisms of phase stability of HEAs is still a topic of active research. Guo and Liu<sup>12</sup> demonstrated that elements likely to form HEAs have near-zero enthalpies of mixing and have very small differences in atomic radius. The small enthalpy of mixing allows the configurational entropy to dominate the free energy, and it has been proposed that the system behaves, in this case, more like an ideal solution. Otto et al.<sup>13</sup> recently published a systematic investigation on the effect of entropy on phase stability of HEAs. The authors demonstrated that high configurational entropy is not the only sufficient criterion to predict whether an equiatomic multicomponent alloy will form as a single-phase solid solution. In their study, they found only NiFeCrCoMn alloys to be a single-phase fcc solid solution and an HEA. These findings are consistent with the work of Guo et al. as all the enthalpies of mixing in the respective binary alloys are relatively small and the atoms are similar in size. The authors then replaced individual elements in an equiatomic NiFeCrCoMn alloy one at a time with elements that have the same room temperature crystal structure, similar atomic size, and similar electronegativity as compared to the elements being replaced. All other substitutions to the NiFeCrCoMn alloy led to a multiphase alloy. Although the replacement elements were “similar” according to Hume–Rothery rules, the authors found that the substituted elements had a stronger propensity to form secondary phases or intermetallics in their respective binary alloys. This led the system to act less as an ideal solution and resulted in the formation of multiphase alloy with a reduced overall entropy.<sup>13</sup>

There has also been interest in finding descriptors to predict the likely lattice that the solid solution will form on. One descriptor that has been reasonably successful in predicting the lattice structure is the average valence electron concentration (VEC).<sup>14</sup> FCC phases were determined to be more stable at higher VEC ( $\geq 8$ ), while body-centered cubic (bcc)

phases were determined to be more stable at lower VEC ( $< 6.87$ ). On the boundary between fcc and bcc (VEC = 8), the systems were found to be predominantly fcc, but in some situations bcc has been seen in minute amounts.

To explore the physical properties of an HEA, we have implemented an integrated approach that combines results from experiment and first-principles electronic structure methods. Ni, Fe, Cr, Co, and Mn were chosen as the components of the HEA studied herein. The small size difference, small enthalpies of mixing, VEC, and previous findings suggest that this forms as a solid solution on the fcc lattice. Additionally, binary (NiFe), ternary (NiFeCr), and quaternary (NiFeCrCo) alloys form fcc solid-solution phases. This allows us to explore the evolution of a variety of properties, such as elastic constants, lattice parameters, and stacking fault energies, as a function of the number of components. We show the atomic radii of these elements from the literature in Table I.

The VEC of NiFeCrCoMn is 8 and is found to be solely fcc in both previous studies and our current work.<sup>13,16</sup>

In addition to the equiatomic alloys, we also produced some off stoichiometry five-component alloys to determine how the SFE and other properties change with composition. The alloys produced for this study are listed in Table II along with their average VEC and the entropy of mixing for the ideal solid solution, given by  $\Delta S = -R \sum x_i \ln x_i$ , where  $R$  is the ideal gas constant and  $x_i$  is the concentration of component  $i$ .

In this article, we have adopted the following naming convention: Alloy names without subscripts are equiatomic; in alloy names with subscripts, the subscript value is the concentration in atomic percent.

## METHODS

### Experimental

Alloy powders were prepared by mechanical alloying of elemental powders in a high-energy ball mill. Powders of better than 99% purity were loaded into a stainless steel vial with stainless steel balls in a high-purity argon atmosphere. A 10:1 ball-to-powder weight ratio was used. Approximately 0.7 wt.% dodecane (two drops) was added to four- and five-component alloys as a process control agent to minimize cold welding. Binary (NiFe) alloys were milled in a modified SPEX 8000 mixer mill (SPEX SamplePrep, Metuchen, NJ, USA) cooled by liquid nitrogen for 4 h. Ternary (NiFeCr) alloys were milled at liquid nitrogen temperatures for 8 h, followed by 17 h of milling at room temperature with forced-air cooling. Quaternary (NiFeCrCo) and quinary (NiFeCrCoMn) samples were milled with forced-air cooling for 24–29 h. Before any analysis, the dodecane was removed by evaporation in a vacuum chamber for at least 18 h.

**Table I. Atomic radii and valence electron concentration of pure metals<sup>15</sup>**

Element	Ni	Fe	Cr	Co	Mn	Average
Atomic radius (pm)	124.6	127.4	128.2	125.2	126.4	126.4
VEC	10	8	6	9	7	8

**Table II. Composition, average VEC, and ideal entropy of mixing of alloys produced**

Alloy	VEC	$\Delta S_{\text{mix}}$ (J K <sup>-1</sup> mol <sup>-1</sup> )
NiFe	9	5.76
NiFeCr	8	9.13
NiFeCrCo	8.25	11.53
NiFeCrCoMn	8	13.38
Ni <sub>26</sub> Fe <sub>20</sub> -Cr <sub>14</sub> Co <sub>20</sub> Mn <sub>20</sub>	8.24	13.23
Ni <sub>23</sub> Fe <sub>20</sub> -Cr <sub>17</sub> Co <sub>20</sub> Mn <sub>20</sub>	8.12	13.34
Ni <sub>14</sub> Fe <sub>20</sub> -Cr <sub>26</sub> Co <sub>20</sub> Mn <sub>20</sub>	7.76	13.23
Ni <sub>14</sub> Fe <sub>21.5</sub> Cr <sub>21.5</sub> Co <sub>21.5</sub> Mn <sub>21.5</sub>	7.85	13.28

Bulk samples were prepared by arc melting. Pure (better than 99%), bulk elements were melted on a water-cooled copper hearth in a Ti-gettered argon atmosphere. Ingots were flipped and remelted at least three times to ensure the elements were well mixed. Samples were drop cast into a water-cooled 7-mm-diameter cylindrical copper mold.

X-ray diffraction (XRD) analysis was conducted using a Rigaku Smartlab diffractometer (Rigaku Corporation, Tokyo, Japan) with Cu K $\alpha$  radiation. The PM2K software was used to analyze the diffraction patterns using the whole powder pattern modeling algorithm.<sup>17</sup> With this method, multiple models relating the microstructure and crystallography of the sample are convoluted and simultaneously refined to fit the measured pattern using a nonlinear least-squares algorithm. The software accounts for instrumental broadening and can correct for sample position errors. PM2K was used to measure the lattice parameter, dislocation density, grain size, twin fault probability, and stacking fault probability.<sup>17</sup> A Lorentzian peak function was fit to each peak in the diffraction profile and the widths used to determine the microstrain using the Williamson–Hall method.<sup>18</sup> The microstrain was converted to mean-square strain as described by Klug and Alexander.<sup>19</sup> The elastic constants were calculated using density functional theory (DFT) as described in the next section. The SFE is then calculated as:

$$\gamma = \frac{K_{111}\omega_0 G_{(111)} a_0 A^{-0.37} \cdot \varepsilon^2}{\pi\sqrt{3} \alpha} \quad (1)$$

where  $K_{111}\omega_0$  is assumed to be a constant 6.6 for all fcc materials,  $G_{(111)}$  is the shear modulus in the (111) plane,  $a_0$  is the lattice parameter,  $A$  is the Zener elastic anisotropy  $2C_{44}/(C - C_{12})$ ,  $\varepsilon^2$  is the mean square microstrain, and  $\alpha$  in the stacking fault probability.<sup>20</sup> XRD measurements for lattice

parameters of the cast alloys were performed after cold rolling to increase the surface area of the sample.

Microhardness tests were conducted on powder samples that were fixed to a glass slide using epoxy then polished. The cast samples were annealed at 1000°C for 24 h, cut using a low-speed diamond saw, mounted in epoxy, and polished. Testing was done with a 50-g load. At least 10 measurements were taken on each sample.

Young's modulus of the as-milled powders was estimated from the reduced Young's modulus determined by nanoindentation using a Hysitron Triboindenter and a load of 5 mN. The samples were prepared as described for microhardness tests. The Young's modulus of the sample is calculated from the reduced modulus using:

$$\frac{1}{E_r} = \left( \frac{1 - \nu^2}{E} \right)_{\text{sample}} + \left( \frac{1 - \nu^2}{E} \right)_{\text{indenter}} \quad (2)$$

The modulus and Poisson's ratio of the indenter were 1140 GPa and 0.07 GPa, respectively. A range of values of the Poisson's ratio for the alloys was obtained computationally.

The grain size of the cast alloys was determined by optical microscopy and the line-intercept method after polishing and etching by immersion in solutions of (I) CuCl<sub>2</sub>, HCl, and methanol, and (II) FeCl<sub>3</sub>, CuCl<sub>2</sub>, HCl, HNO<sub>3</sub>, and ethanol for the NiFeCrCo and NiFeCrCoMn alloys, respectively.

## Computational

Two methods were used to investigate the physical properties of these solid-solution alloys. Both are based on DFT. The first method was the exact

muffin-tin orbital (EMTO)<sup>21,22</sup> method combined with the coherent potential approximation (CPA).<sup>23,24</sup> The second method was a plane wave-pseudopotential approach as implemented in the Vienna ab initio simulation packages (VASP) version 5.2.12.<sup>25–28</sup> VASP uses periodic boundary conditions. To best approximate the random solid solution, special quasi-random structures (SQSs)<sup>29</sup> were generated using the tool in the alloy theoretic automated toolkit (ATAT).<sup>30</sup>

The EMTO method is an improved screened Korringa–Kohn–Rostoker (KKR) method that uses optimized overlapping muffin-tin potentials to describe the actual crystal potential and calculates system energies with higher accuracy than the conventional muffin-tin orbital (MTO) method.<sup>31</sup> This method is combined with the CPA technique to treat systems with substitutional disorder. The EMTO-CPA method proved a powerful tool in the ab initio study of solid solutions, e.g., mechanical properties<sup>32</sup> and stacking fault energies<sup>33</sup> of stainless steels. In the current EMTO-CPA calculation of HEAs, the one-electron equations were solved using the frozen-core approximation. The Green's function was calculated for 16 complex energy points. The basis set included *s*, *p*, *d*, and *f* orbitals. The Perdew, Burke, and Ernzerhof (PBE) version of generalized gradient approximation (GGA), exchange–correlation functional was applied.<sup>34,35</sup> The magnetic disorder in HEAs was treated by the disordered local moments (DLM) method.<sup>36</sup>

To consider the influence of the lattice displacement on DFT calculations, we also performed similar calculations using VASP + SQS. Projector augmented-wave (PAW) pseudopotentials<sup>37,38</sup> and the PBE version of generalized gradient approximation (GGA-PBE) were used in VASP calculations. There are 10, 8, 6, 9, and 7 valence electrons for elements Ni, Fe, Cr, Co, and Mn, respectively. In addition to these valence electrons, the 3*p* electrons of Fe, Cr, and Mn are also treated explicitly in the PAW pseudopotentials used in this work. Noncollinear spin and spin–orbit coupling was included in the VASP calculations. Both spin-aligned and random moments are assigned to atoms within the SQS. The lowest energy is found to be ferromagnetic at 0 K, which differs from the experimentally measured paramagnetic state. The impact of the ferromagnetism in the predicted properties of VASP will be discussed. The cut-off energy for plane waves was set to 350 eV for all calculations. The *k*-point mesh was selected based on what converged the total energy to  $\sim 1$  meV/atom. This resulted in a  $7 \times 4 \times 4$  and  $4 \times 7 \times 7$   $\Gamma$ -centered mesh for the 24 atom and 20 atom SQSs, respectively. The SQSs were generated by *mcsqs* algorithm included in the ATAT package. The generation of a SQS was based on lattice geometry, specifically the pair correlation function between lattice sites. Different atomic configurations were created and the sum of pair correlation functions on each site was calculated. A

structure in which the sum of pair correlation functions on each site is closer to zero was considered a better SQS. The SQSs of the quaternary and quinary alloys contained 24 atoms and 20 atoms, respectively. Table III contains the atomic positions and site populations for the four- and five-component fcc SQSs used in this work.

There are 46- and 90-pair (out to third nearest neighbor) and triplet (out to second nearest neighbor) correlation functions to report for the four- and five-component systems presented in Table III. We note that none of the absolute magnitudes of the pair correlation function exceed 0.05 and 0.03 for the four- and five-component SQSs, respectively, and none of the triplet correlation functions exceed an absolute magnitude of 0.04 and 0.06 for the four- and five-component SQSs, respectively. The weighted average of the pair and triplet correlation functions were at least one order of magnitude less than these reported maximum values. Although the SQSs contain a small number of atoms, these structures have proven to provide a means to accurately predict physical and elastic properties of alloys.<sup>39,40</sup>

Both methods were used to determine the lattice constant, elastic constants, and Poisson's ratio for the alloys studied herein. The lattice constants for each alloy from DFT calculations are compared to experimental results from our research and the literature. The elastic constants were used to determine the first-principles polycrystalline elastic properties, e.g., Young's modulus and Poisson's ratio. Together with the experimental results, the Poisson's ratio was applied for the measurement of the Young's modulus with Eq. 2. As many of the SFEs are small, the relative energies between important phases used in the axial interaction method to predict SFEs<sup>41,42</sup> [fcc, hexagonal close packed (hcp), and double hexagonal close packed (dhcp)] are also expected to lead to small differences in energy. When this is the case, factors such as zero point energy differences may play a more significant role in the prediction of the SFE. To avoid the added computational expense of these vibrational calculations, we calculate the SFEs by combining experimental measurements from XRD with the predicted elastic properties through Eq. 1. Explicit calculation of the SFEs will be fully explored in a separate publication.

## RESULTS AND DISCUSSION

### X-Ray Diffraction

Figure 1 shows the XRD patterns of the as-milled equiatomic alloys and the Ni<sub>14</sub>Fe<sub>20</sub>Cr<sub>26</sub>Co<sub>20</sub>Mn<sub>20</sub> alloy. All of the alloys are single-phase and fcc. Despite the average VEC of the Ni<sub>14</sub>Fe<sub>20</sub>Cr<sub>26</sub>Co<sub>20</sub>Mn<sub>20</sub> alloy being less than 8, it still forms a single-phase fcc solid solution by mechanical alloying.

**Table III. SQS For NiFeCrCo and NiFeCrCoMn alloys containing 24 atoms and 20 atoms, respectively**

	NiFeCrCo ( $N = 24$ )	NiFeCrCoMn ( $N = 20$ )
Lattice vectors	(0.5, -0.5, -1.0) (-1.5, -1.5, 0.0) (-1.5, 1.5, -1.0)	(0.5, 2.0, -0.5) (0.5, -0.5, 2.0) (1.0, -0.5, -0.5)
Atomic positions	(-1.5, -1.0, -1.5) Ni (-2.0, 0.5, -1.5) Ni (-1.5, 0.5, -2.0) Ni (-1.5, 0.5, -1.0) Ni (-0.5, -0.5, -1.0) Ni (-0.5, 0.0, -0.5) Ni (-2.5, 0.0, -1.5) Fe (-1.0, -1.0, -1.0) Fe (-1.0, 0.0, -1.0) Fe (-1.5, 1.0, -1.5) Fe (-2.5, -0.5, -2.0) Fe (-1.0, 0.5, -1.5) Fe (-2.0, 0.0, -2.0) Cr (-2.0, 0.0, -1.0) Cr (-1.5, -0.5, -1.0) Cr (-1.0, -0.5, -1.5) Cr (-1.0, -0.5, -0.5) Cr (-2.5, -0.5, -1.0) Cr (-1.5, -1.0, -0.5) Co (-2.0, -0.5, -1.5) Co (-1.5, 0.0, -1.5) Co (-0.5, 0.0, -1.5) Co (-2.0, -1.0, -1.0) Co (-1.5, -1.5, -1.0) Co	(0.5, 0.0, 0.5) Ni (1.0, 0.5, 1.5) Ni (1.0, 0.5, -0.5) Ni (1.5, 0.0, 0.5) Ni (1.0, -0.5, 0.5) Fe (1.0, 1.5, 0.5) Fe (1.5, -0.5, 1.0) Fe (1.5, 0.5, 0.0) Fe (1.0, 1.5, -0.5) Cr (1.5, 0.5, 1.0) Cr (1.5, 1.0, -0.5) Cr (1.5, 1.0, 0.5) Cr (0.5, 0.5, 0.0) Co (1.0, 0.5, 0.5) Co (1.0, 1.0, 1.0) Co (1.0, 1.0, 0.0) Co (1.0, -0.5, 1.5) Mn (1.0, 0.0, 1.0) Mn (1.0, 0.0, 0.0) Mn (2.0, 1.0, 1.0) Mn

Lattice vectors and atomic positions are given in Cartesian coordinates, in units of  $a$ , the fcc lattice parameter. Atomic positions are given for the ideal, unrelaxed fcc sites

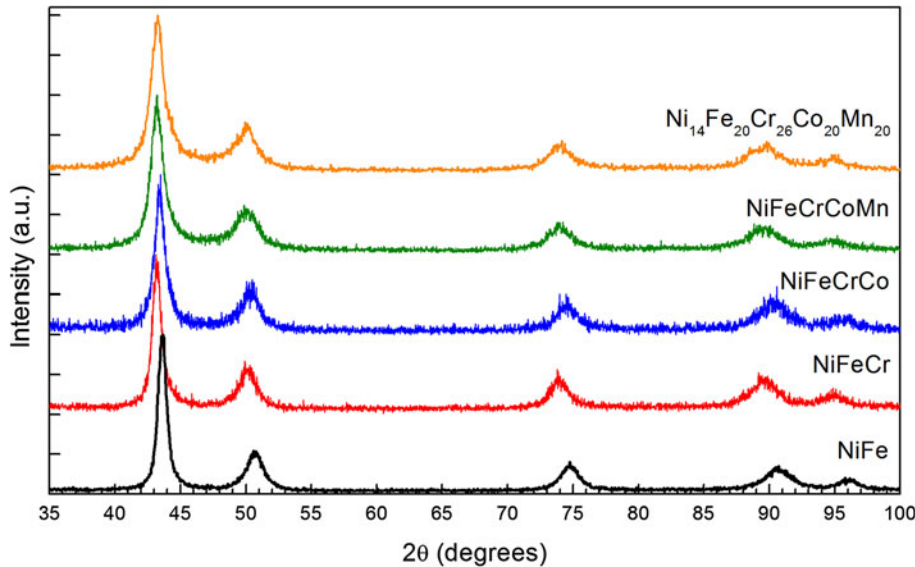


Fig. 1. XRD patterns of as-milled equiatomic NiFe, NiFeCr, NiFeCrCo, and NiFeCrCoMn.

The lattice parameters of the four and five components were determined directly from the XRD measurements and first-principles calculations. For NiFeCrCo, the lattice parameters measured by XRD were 3.613 Å and 3.575 Å for the as-milled and cast

samples, respectively. First-principles calculations predict lattice parameters of 3.58 Å and 3.54 Å from EMTO-CPA and VASP + SQS methods, respectively. Both results are within 1% of the cast results and are consistent with the measured lattice

parameters presented in Ref. 43. For the NiFeCrCoMn alloy, the lattice parameters from XRD were measured to be 3.624 Å and 3.597 Å for the as-milled and cast samples, respectively. The trends in both first principles agree with the experimental trend of increasing lattice parameter with increasing the number of components. The lattice parameter predictions for NiFeCrCoMn from first-principles calculations were 3.60 Å and 3.54 Å for EMTO-CPA and VASP + SQS methods, respectively, with the error on the order of 1.6% relative to the cast lattice parameter. The lattice parameter for the off stoichiometry  $\text{Ni}_{14}\text{Fe}_{20}\text{Cr}_{26}\text{Co}_{20}\text{Mn}_{20}$  alloy is found to be 3.627 Å and 3.60 Å from XRD of the as-milled alloy and EMTO-CPA, respectively, which is an error of 0.7%. The lattice parameters of the as-milled alloys are expected to be higher as a result of the nonequilibrium processing conditions and high defect density.<sup>44</sup>

### Single-Crystal Elastic Constants

The elastic properties of a crystal can be expressed by the elasticity tensor. For cubic structures, there are three independent elastic constants  $C_{11}$ ,  $C_{12}$ , and  $C_{44}$ .  $C_{11}$ , and  $C_{12}$  can be derived from the bulk modulus  $B$  and the tetragonal shear modulus  $C'$ , given that  $B = (C_{11} + 2C_{12})/3$  and  $C' = (C_{11} - C_{12})/2$ . The bulk modulus was obtained by fitting the energy-volume data to the Birch-Murnaghan equation of state. For the tetragonal shear modulus  $C'$  and  $C_{44}$ , we applied a volume-conserving orthorhombic deformation  $\varepsilon_0$  and a volume-conserving monoclinic deformation  $\varepsilon_m$  on the fcc lattice,<sup>38</sup> respectively. These relationships are:

$$\varepsilon_0 = \begin{pmatrix} 1 + \delta & 0 & 0 \\ 0 & 1 - \delta & 0 \\ 0 & 0 & (1 - \delta^2)^{-1} \end{pmatrix}; \quad (3)$$

$$\varepsilon_m = \begin{pmatrix} 1 & \delta & 0 \\ \delta & 1 & 0 \\ 0 & 0 & (1 - \delta^2)^{-1} \end{pmatrix}$$

where  $\delta$  was between 0.00 and 0.05 in increments of 0.01. The values of  $C'$  and  $C_{44}$  were determined by fitting the calculated energies to  $E = E_0 + 2VC'\delta^2$  and  $E = E_0 + 2VC_{44}\delta^2$ .<sup>45</sup> In these expressions,  $E$  is the total energy of the strained system from first principles,  $E_0$  is the energy at the equilibrium volume, and  $V$  is the volume of the cell. The elastic constants were determined using EMTO-CPA and VASP for NiFeCrCo and NiFeCrCoMn, while the elastic constants for off stoichiometry alloys were determined from EMTO-CPA alone. A strain range no greater than 5% was used in the EMTO-CPA and the VASP calculations to determine the bulk modulus through fitting of results to the Birch-Murnaghan equations of state. As shown in Fig. 2, the calculated elastic constants and bulk moduli

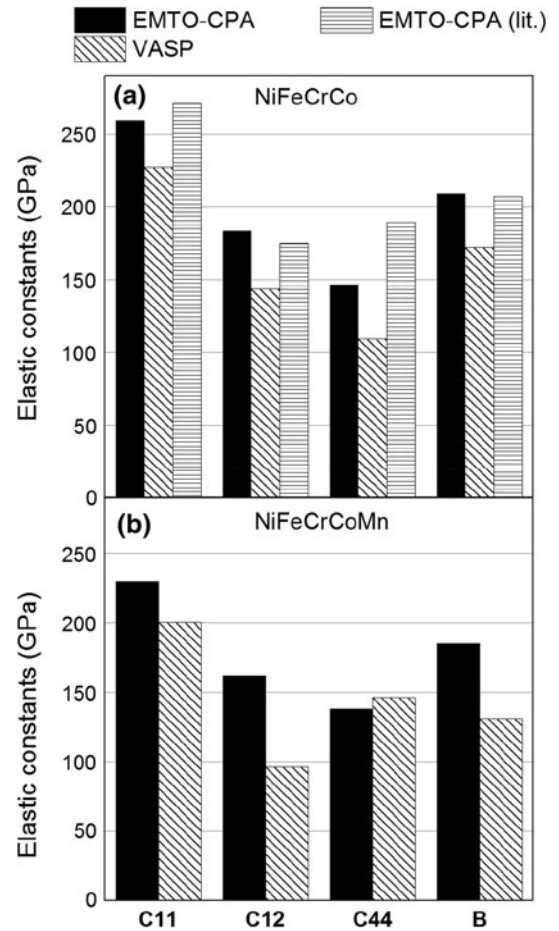


Fig. 2. Elastic constants of equiatomic NiFeCrCo (a) and NiFeCrCoMn (b).<sup>46</sup>

depend on the first-principles method implemented. The deviation between the results of the two methods increases for NiFeCrCoMn. We also compare our results of the four-component systems to Tian et al.<sup>46</sup> who calculated the elastic constants of NiFeCrCo using the EMTO-CPA code. The differences between our results and those published are small and attributed to the setup of the calculations. Tian et al. used soft core, 240  $k$ -points, and a screening parameter of 0.6. In our calculations we implemented frozen core, 419  $k$ -points, and a screening parameter of 0.9.

Deviations in the elastic constants between VASP and EMTO-CPA for the four- and five-component alloys were explored and are believed to be partially due to the magnetic configuration in the calculation. VASP predicts ferromagnetic, while EMTO-CPA is run with DLM approximating the paramagnetic state. To the validity of this assertion, EMTO-CPA was run with a ferromagnetic configuration. This ferromagnetic EMTO-CPA calculation predicts a lower total energy at 0 K and elastic coefficients in closer agreement to the VASP calculations. The

elastic constants from our EMTO-CPA and VASP calculations will be used to determine polycrystalline constants, which will then be used with Eq. 1 to determine the SFEs of the alloys. Although there are differences in the predicted elastic constants, it will be shown that these have a smaller impact on the SFEs determined by this process.

### Polycrystalline Elastic Constants

We derived the polycrystalline elastic properties using the elastic constants and the Voigt–Reuss (V–R) averaging method.<sup>47</sup> According to the V–R method, the polycrystalline bulk modulus is the same as the single crystalline bulk modulus from DFT calculation, while the shear modulus  $G$  can be given by the upper ( $G_V$ ) and lower ( $G_R$ ) bounds:

$$G_V = \frac{(C_{11} - C_{12} + 3C_{44})}{5}; \quad (4)$$

$$G_R = \frac{5(C_{11} - C_{12})C_{44}}{4C_{44} + 3(C_{11} - C_{12})}$$

The shear modulus  $G$  can be estimated as  $(G_V + G_R)/2$ , according to the Hill averaging method.<sup>43</sup> Poisson's ratio and Young's modulus  $E$  for an isotropic material can be derived from the bulk modulus  $B$  and shear modulus  $G$ :

$$\nu = \frac{3B - 2G}{2(3B + G)}; E = \frac{9BG}{3B + G} \quad (5)$$

Table IV shows the calculated values of Poisson's ratio assuming a Hill average.

The values of Poisson's ratio of NiFeCrCo from the two first-principles methods are very close. As noted previously, the elastic constants of NiFeCrCo from the two methods differ, which is not surprising as there are differences in the bulk modulus (208 GPa vs. 171 GPa from EMTO and VASP, respectively). This implies that the deviations of the elastic constants are cancelled during the calculation of Poisson's ratio in Eqs. 4 and 5. The Hill average of Poisson's ratio of NiFeCrCoMn differs as much as  $\sim 42\%$  between the two methods, which arises from the deviation of elastic constants. As noted previously, this may be partially related to the differences in the magnetic state.

Table V shows the values of Young's modulus from our calculations and experiments.

The range of values from the nanoindentation experiments was determined by converting the reduced modulus using the Hill average of Poisson's ratio from the DFT calculations. VASP and EMTO results are presented for the four-component alloy, but only EMTO-CPA results are included for the five-component alloy. While there is closer agreement between theory and experiment for the NiFeCrCo alloy, the measured Young's modulus of the

**Table IV. Poisson's ratio of NiFeCrCo and NiFeCrCoMn from DFT calculations**

	Hill average
NiFeCrCo (EMTO-CPA)	0.319
NiFeCrCo (VASP)	0.311
NiFeCrCoMn (EMTO-CPA)	0.313
NiFeCrCoMn (VASP)	0.204

**Table V. Young's modulus of NiFeCrCo and NiFeCrCoMn from DFT calculations and experiment**

	$E_{\text{Hill}}$ (GPa)
NiFeCrCo (EMTO-CPA)	225
NiFeCrCo (VASP)	195
NiFeCrCo (nanoindentation + EMTO)	171
NiFeCrCo (nanoindentation + VASP)	172
NiFeCrCoMn (EMTO-CPA)	207
NiFeCrCoMn (nanoindentation + EMTO)	137

NiFeCrCoMn alloy is substantially lower than the predicted result. It should be noted that the bulk moduli calculated using VASP for the four- and five-component alloys presented previously in Fig. 2 show a decrease in the bulk modulus from 172 GPa to 131 GPa. With a more physical Poisson's ratio for the five-component alloy (i.e., closer to the 0.311 predicated for the four-component alloy) and the following relationship between Bulk modulus and Young's modulus for an isotropic solid:  $E = 3B(1 - 2\nu)$ , we would find these results closer to experiment with Young's moduli of 195 GPa and 149 GPa for the four- and five-component alloys, respectively. Due to the scatter in the measurement of the reduced modulus, we consider these in good agreement with experimental measurements from nanoindentation.

### Stacking Fault Energy

Figure 3 shows the ratio of the mean square microstrain to the stacking fault probability in the as-milled alloys as measured using XRD. From Eq. 1, this value is related to the SFE by the elastic constants and the lattice parameter. From these results, we can predict that the SFE of the four- and five-component alloys will be nearly an order of magnitude lower than that of NiFe.

Table VI shows the SFE of the four- and five-component alloys measured using the x-ray stacking fault probability and elastic constants determined by VASP and EMTO-CPA.

No reliable error values can be determined for the measurements. The PM2K software calculates an estimated standard deviation for the stacking fault probability and lattice parameter. Nevertheless,

there is likely significant error associated with the microstrain calculation, but the Williamson–Hall method does not provide a way to quantify it. Despite significant differences in the elastic constants of the four-component alloy as determined by VASP and EMTO-CPA, the SFE measurements agree to within  $0.005 \text{ mJ/m}^2$ , which is within the measurement limits. As with the Poisson's ratio calculation, there is cancellation of error in these measurements.

Figure 4 compares the averages of the measured SFE of the NiFe, NiFeCr, NiFeCrCo, and NiFeCrCoMn alloys produced in this study to literature values of pure Ni and NiFe. The elastic constants used for the XRD measurements of NiFe are from Ref. 48. From these measurements, we can conclude that the multicomponent alloys have relatively low stacking fault energies valued at less than a quarter of the SFE of pure nickel. Nevertheless, these values are still on the same order as or slightly higher than some conventional austenitic stainless steel alloys such as AISI 304L ( $\gamma = 18 \text{ mJ/m}^2$ ) and AISI 305 ( $\gamma = 34 \text{ mJ/m}^2$ ).<sup>50</sup> Additionally, the decrease in SFE is smaller with each additional alloying element, suggesting that simply adding more elements may not lead to a substantial reduction of the SFE. These results show that while equiatomic NiFeCrCoMn alloys do have reduced SFE, obtaining SFEs on the order of those seen in common copper alloys ( $< 15 \text{ mJ/m}^2$ ) will require finding an optimum composition or compositions. This is a difficult problem

considering the number of elements and the wide range of compositions that are still considered HEAs.

As Ni is known to have a high SFE, we explored varying its composition while increasing composition of other components in the HEA. We mainly increase the composition of Cr as Ni content is reduced, but we also explored raising the composition of all components for a reduced Ni concentration. Figure 5 shows the ratio of the mean square microstrain to the stacking fault probability in the as-

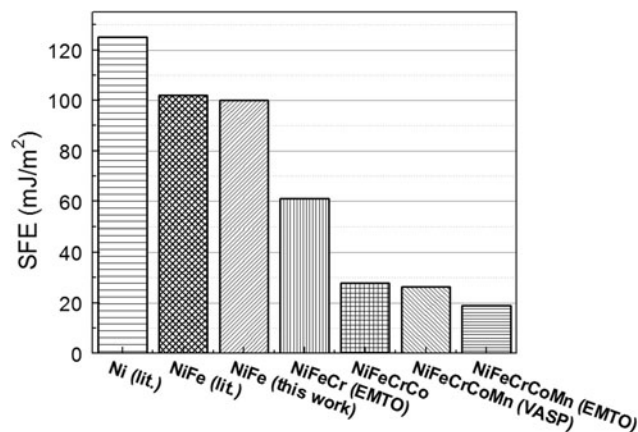


Fig. 4. SFEs of equiatomic fcc metals from pure Ni to NiFeCrCoMn.<sup>20,49</sup>

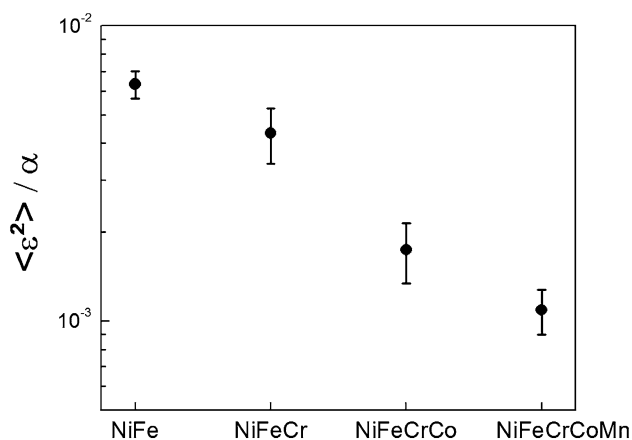


Fig. 3. Ratio of mean-square microstrain to stacking fault probability for NiFe, NiFeCr, NiFeCrCo, and NiFeCrCoMn. Error bars represent error from the stacking fault probability measurement.

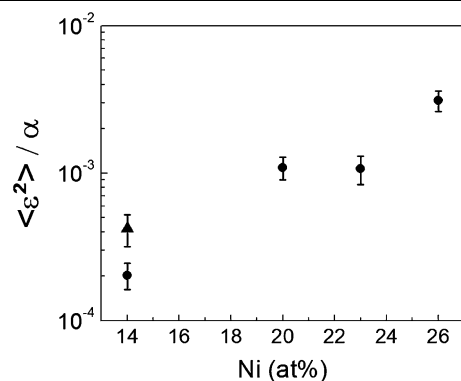


Fig. 5. Ratio of mean-square microstrain to stacking fault probability for five-component alloys. Error bars represent error from the stacking fault probability measurement. Circles represent the alloys in which Cr balances the difference in Ni content. The triangle is the alloy in which the concentrations of all other elements are increased equally to balance the Ni.

**Table VI. SFEs of NiFeCrCo and NiFeCrCoMn calculated from experimental data of stacking fault probability and DFT calculations of elastic constants**

Alloy	SFE (mJ/m <sup>2</sup> ) (VASP)	SFE (mJ/m <sup>2</sup> ) (EMTO-CPA)
NiFeCrCo-1	17.4	17.4
NiFeCrCo-2	34.3	34.3
NiFeCrCo-3	31.7	31.7
NiFeCrCoMn-1	27.3	19.6
NiFeCrCoMn-2	25.5	18.3



milled five-component alloys as a function of Ni concentration. From this data, it is expected that the low-Ni alloys will have a much lower SFE than the equiatomic alloy. The SFEs of the nonequiatomic alloys, using elastic constants calculated by EMTO-CPA, are listed in Table VII.

From these results, we can see that there is a dependence on both the Ni and Cr concentrations. While lowering the Ni concentration independently of the Cr does significantly reduce the SFE, it does not do so to the same extent as reducing Ni and increasing Cr. The  $\text{Ni}_{14}\text{Fe}_{20}\text{Cr}_{26}\text{Co}_{20}\text{Mn}_{20}$  alloy has an extremely low SFE, apparently even lower than Cu-Al-Zn<sup>51</sup> and Cu-Ge<sup>2</sup> alloys. The SFE of various conventional alloys known to have a low SFE are compared to the HEAs from this study in Fig. 6.

**Table VII. SFE of nonequiatomic HEAs**

Alloy	SFE ( $\text{mJ}/\text{m}^2$ )
$\text{Ni}_{26}\text{Fe}_{20}\text{Cr}_{14}\text{Co}_{20}\text{Mn}_{20}$	57.7
$\text{Ni}_{23}\text{Fe}_{20}\text{Cr}_{17}\text{Co}_{20}\text{Mn}_{20}$	19.7
$\text{Ni}_{14}\text{Fe}_{20}\text{Cr}_{26}\text{Co}_{20}\text{Mn}_{20}$	3.5
$\text{Ni}_{14}\text{Fe}_{21.5}\text{Cr}_{21.5}\text{Co}_{21.5}\text{Mn}_{21.5}$	7.7

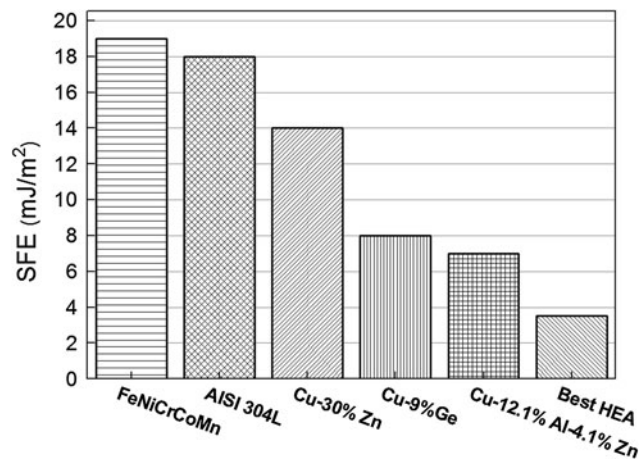


Fig. 6. SFEs of equiatomic NiFeCrCoMn and  $\text{Ni}_{14}\text{Fe}_{20}\text{Cr}_{26}\text{Co}_{20}\text{Mn}_{20}$  (best HEA) compared to other low SFE alloys.<sup>2,50,51</sup>

## Mechanical Properties

Gali and George<sup>52</sup> conducted a detailed study of the tensile properties of hot-rolled and annealed NiFeCrCo and NiFeCrCoMn. They measured room temperature yield strengths of  $\sim 200$  MPa in the four-component alloy and  $\sim 300$  MPa in the five-component alloy with grain sizes of  $14 \mu\text{m}$  and  $35 \mu\text{m}$ , respectively. They also measured uniform elongation of  $\sim 40\%$  at room temperature and found that as the test temperature decreased to  $-196^\circ\text{C}$ , both the strength and ductility increased. Annealing twins were observed and a high work hardening rate was attributed to the formation of nanoscale deformation twins.<sup>52</sup>

Hardness and grain size measurements from the as-milled powders and cast alloys of this study are shown in Table VIII.

Measurement of the grain size of the five-component alloy was difficult due to the large numbers of annealing twins. Additionally, the twin fault probability as measured by XRD in the as-milled four- and five-component samples was found to be very high, on the order of 0.1. The hardness results show that the NC alloys have extremely high strength. Using the common empirical  $\text{HV} = 3\sigma_y$  relation, the yield strength is likely in the range of 2–2.5 GPa. These results, and those from earlier studies, are consistent with our measurements of low SFE.

## SUMMARY

The elastic properties and stacking fault energies of multicomponent alloys containing Ni, Fe, Cr, Co, and Mn were determined using a combination of DFT calculations and experiments. Reasonable agreement between experiments and calculation was found for the lattice parameter and elastic properties, although further experimental work is required to measure values that are completely independent of the calculations. The SFE of the equiatomic NiFeCrCo and NiFeCrCoMn alloys measured by XRD is approximately  $20 \text{ mJ}/\text{m}^2$  to  $25 \text{ mJ}/\text{m}^2$ , which is substantially lower than that of pure Ni and NiFe. These measurements are in agreement with the results of mechanical testing and microstructure characterization by XRD. By altering the composition, the SFE can be tailored to a wide range of values, including low values comparable to or better than conventional low SFE alloys. The results indicate that fcc HEAs such as NiFeCrCoMn can be engineered to have both high

**Table VIII. Hardness and grain size measurements from the as-milled powders and cast alloys**

Material	Hardness (GPa)	Grain size	Std. Dev. of grain size
As-milled NiFeCrCo	$6.3 \pm 0.1$	22 nm	9 nm
As-milled NiFeCrCoMn	$7.8 \pm 0.2$	9.4 nm	5 nm
Cast NiFeCrCo	$1.66 \pm 0.07$	$20 \mu\text{m}$	–
Cast NiFeCrCoMn	$1.42 \pm 0.03$	$49 \mu\text{m}$	–

strength and ductility, making them promising candidates for future use as structural materials.

### ACKNOWLEDGEMENTS

The work reported in this manuscript was made possible through support from the National Science Foundation from the Metals and Metallic Nanostructures program under grant DMR-1104930. D.L.I. and C.N. would also like to acknowledge Levente Vitos for sharing his EMTO-CPA code for work on this project.

### REFERENCES

1. Y.H. Zhao, Y.T. Zhu, X.Z. Liao, Z. Horita, and T.G. Langdon, *Appl. Phys. Lett.* 89, 121906 (2006).
2. Y.L. Gong, C.E. Wen, Y.C. Li, X.X. Wu, L.P. Cheng, X.C. Han, and X.K. Zhu, *Mater. Sci. Eng. A* 569, 144 (2013).
3. P.-L. Sun, Y.H. Zhao, J.C. Cooley, M.E. Kassner, Z. Horita, T.G. Langdon, E.J. Lavernia, and Y.T. Zhu, *Mater. Sci. Eng. A* 525, 83 (2009).
4. K. Youssef, M. Sakaliyska, H. Bahmanpour, R. Scattergood, and C. Koch, *Acta Mater.* 59, 5758 (2011).
5. H. Bahmanpour, A. Kauffmann, M.S. Khoshkhou, K.M. Youssef, S. Mula, J. Freudenberger, J. Eckert, R.O. Scattergood, and C.C. Koch, *Mater. Sci. Eng. A* 529, 230 (2011).
6. Z.W. Wang, Y.B. Wang, X.Z. Liao, Y.H. Zhao, E.J. Lavernia, Y.T. Zhu, Z. Horita, and T.G. Langdon, *Scripta Mater.* 60, 52 (2009).
7. X.H. An, Q.Y. Lin, S.D. Wu, Z.F. Zhang, R.B. Figueiredo, N. Gao, and T.G. Langdon, *Scripta Mater.* 64, 954 (2011).
8. G.E. Dieter, *Mechanical Metallurgy*, 3rd ed. (New York: McGraw-Hill, 1986), pp. 135–157.
9. Y. Zhang, N.R. Tao, and K. Lu, *Scripta Mater.* 60, 211 (2009).
10. W.W. Jian, G.M. Cheng, W.Z. Xu, H. Yuan, M.H. Tsai, Q.D. Wang, C.C. Koch, Y.T. Zhu, and S.N. Mathaudhu, *Mater. Res. Lett.* 1, 61 (2013).
11. J.-W. Yeh, S.-K. Chen, S.-J. Lin, J.-Y. Gan, T.-S. Chin, T.-T. Shun, C.-H. Tsau, and S.-Y. Chang, *Adv. Eng. Mater.* 6, 299 (2004).
12. S. Guo and C. Liu, *Prog. Nat. Sci.: Mater. Int.* 21, 433 (2011).
13. F. Otto, Y. Yang, H. Bei, and E.P. George, *Acta Mater.* 61, 2628 (2013).
14. S. Guo, C. Ng, J. Lu, and C.T. Liu, *J. Appl. Phys.* 109, 103505 (2011).
15. R.J.D. Tilley, *Understanding Solids: The Science of Materials* (Hoboken: Wiley, 2004).
16. B. Cantor, I.T.H. Chang, P. Knight, and A.J.B. Vincent, *Mater. Sci. Eng. A* 375–377, 213 (2004).
17. M. Leoni, T. Confente, and P. Scardi, *Z. Kristallogr* 23, 249 (2006).
18. G.K. Williamson and W.H. Hall, *Acta Metall.* 1, 22 (1953).
19. H.P. Klug and L.E. Alexander, *X-Ray Diffraction Procedures for Polycrystalline and Amorphous Materials*, 2nd ed. (New York: Wiley, 1974), pp. 660–662.
20. R.E. Schramm and R.P. Reed, *Metall. Trans. A* 7A, 359 (1976).
21. L. Vitos, *Phys. Rev. B* 64, 014107 (2001).
22. L. Vitos, *Computational Quantum Mechanics for Materials Engineers: The EMTO Method and Applications* (London: Springer, 2007).
23. P. Soven, *Phys. Rev.* 156, 809 (1967).
24. L. Vitos, I. Abrikosov, and B. Johansson, *Phys. Rev. Lett.* 87, 156401 (2001).
25. G. Kresse and J. Hafner, *Phys. Rev. B* 47, 558 (1993).
26. G. Kresse and J. Furthmüller, *Phys. Rev. B* 54, 11169 (1996).
27. G. Kresse and J. Furthmüller, *Comput. Mater. Sci.* 6, 15 (1996).
28. G. Kresse and J. Hafner, *Phys. Rev. B* 49, 14251 (1994).
29. A. Zunger, S.-H. Wei, L.G. Ferreira, and J.E. Bernard, *Phys. Rev. Lett.* 65, 353 (1990).
30. A. van de Walle, M. Asta, and G. Ceder, *CALPHAD* 26, 539 (2002).
31. O. Andersen, O. Jepsen, and G. Krier, *Lectures on Methods of Electronic Structure Calculations*, ed. V. Kumar, O.K. Andersen, and A. Mookerjee (Singapore: World Scientific, 1994).
32. L. Vitos, P. Korzhavyi, and B. Johansson, *Phys. Rev. Lett.* 88, 13 (2002).
33. L. Vitos, P.A. Korzhavyi, J.-O. Nilsson, and B. Johansson, *Phys. Scripta* 77, 065703 (2008).
34. J. Perdew, K. Burke, and M. Ernzerhof, *Phys. Rev. Lett.* 77, 3865 (1996).
35. J. Perdew, K. Burke, and M. Ernzerhof, *Phys. Rev. Lett.* 78, 1396 (1997).
36. B.L. Gyorffy, A.J. Pindor, J. Staunton, G.M. Stocks, and H. Winter, *J. Phys. F: Met. Phys.* 15, 1337 (1985).
37. P. Blöchl, *Phys. Rev. B* 50, 17953 (1994).
38. G. Kresse and D. Joubert, *Phys. Rev. B* 59, 1758 (1999).
39. C. Jiang, L. Chen, and Z.-K. Liu, *Acta Mater.* 53, 2643 (2005).
40. J. Pezold, A. Dick, M. Friák, and J. Neugebauer, *Phys. Rev. B* 81, 094203 (2010).
41. S. Lu, Q.-M. Hu, E.K. Delczeg-Czirjak, B. Johansson, and L. Vitos, *Acta Mater.* 60, 4506 (2012).
42. L. Vitos, J.-O. Nilsson, and B. Johansson, *Acta Mater.* 54, 3821 (2006).
43. M.S. Lucas, L. Mauger, J.A. Muñoz, Y. Xiao, A.O. Sheets, S.L. Semiatin, J. Horwath, and Z. Turgut, *J. Appl. Phys.* 109, 07E307 (2011).
44. S. Vives, E. Gaffet, and C. Meunier, *Mater. Sci. Eng. A* 336, 229 (2004).
45. M.J. Mehl, J.E. Osburn, D.A. Papaconstantopoulos, and B.M. Klein, *Phys. Rev. B* 41, 10311 (1990).
46. F. Tian, L.K. Varga, N. Chen, L. Delczeg, and L. Vitos, *Phys. Rev. B* 87, 075144 (2013).
47. G. Grimvall, *Thermophysical Properties of Materials* (Amsterdam: North-Holland, 1999).
48. H.M. Ledbetter and R.P. Reed, *J. Phys. Chem. Ref. Data* 2, 531 (1973).
49. C.B. Carter and S.M. Holmes, *Philos. Mag.* 35, 1161 (1977).
50. R.E. Schramm and R.P. Reed, *Metall. Trans. A* 6, 1345 (1975).
51. M.F. Denanot and J.P. Villain, *Phys. Status Solidi A* 8, K125 (1971).
52. A. Gali and E.P. George, *Intermetallics* 39, 74 (2013).